INSTITUTE OF PHYSICS PUBLISHING JOURNAL OF OPTICS A: PURE AND APPLIED OPTICS
J. Opt. A: Pure Appl. Opt. **8** (2006) 363–372 doi:10.1088/1464-4258/8/5/001

Chiral conical diffraction

M V Berry and M R Jeffrey

H H Wills Physics Laboratory, Tyndall Avenue, Bristol BS8 1TL, UK

Received 12 December 2005, accepted for publication 6 January 2006
Published 21 March 2006
Online at stacks.iop.org/JOptA/8/363

Abstract
The geometrical and wave optics are explored for light emerging from a slab of transparent biaxial crystal with optical activity (chirality), for an incident beam directed along the optic axis. The geometrical optics, here derived from Hamilton's principle, is dominated by a circularly symmetric cusped caustic surface ('spun cusp') threaded by an axial focal line. In wave optics, formulated exactly in the paraxial approximation in terms of integrals previously obtained by Belsky and Stepanov and here derived using a unitary evolution operator, the field is determined by two dimensionless parameters. The geometrical features are decorated by interference, here explored in the focal image plane (where the Poggendorff rings of the non-chiral case are in sharpest focus) and along the axis. Asymptotic approximations are derived in terms of the geometrical optics rays (including interference and evanescent waves), near the spun cusp, and uniformly across the caustic surface far from the cusp.

Keywords: polarization, birefringence, chirality, crystal optics

1. Introduction

175 years after Hamilton's discovery of conical refraction [1–3], this remarkable optical singularity is now understood in all its details, theoretically [4, 5] and experimentally [6]. These studies reveal a rich interplay between geometrical rays and polarized waves (hence our term conical diffraction). Hamilton considered a biaxial transparent crystal without optical activity. Obvious extensions are to crystals that are optically active and absorbing. We can expect different physics in these cases, because each extension radically changes the mathematical structure of the spectral problem underlying crystal optics [7–9]: chirality changes the dielectric matrix from real symmetric to complex Hermitian, and absorption destroys hermiticity [10].

Here we consider the first extension, by giving a detailed theory of optical beams transmitted by transparent optically active birefringent crystals. The aim is to describe the structure of the light field in the space beyond the crystal, including its virtual extension backwards within and in front of the crystal (which can be lensed onto an observation screen [6]). The surprising outcome is that the field is dominated by a bright caustic surface formed by rotating a cusped curve about the symmetry axis—a 'spun cusp'; the spun cusp is threaded by an axial focal line. This contrasts sharply with the non-chiral case, where the principal features are two bright rings separated by the Poggendorff dark ring [11, 12], which is an 'anti-caustic' [5].

Previous studies of chiral conical diffraction have missed the dominant features. Early theories [13, 14] were largely geometrical, concentrating on the details of the wave surface and on the azimuthal polarization pattern. Experiments have been performed [15] on α-iodic acid, supported by an approximate theoretical analysis, studying the field at the exit face of the crystal. Definitive formulation of the theory was achieved only recently by Belsky and Stepanov [16], in terms of three diffraction integrals. It is the rich physical content of this theory that we explore here.

The most fundamental procedure is to develop the theory starting from Maxwell's equations, but we choose a simpler route, incorporating from the start the fact that in all cases known to us the deviations from isotropy are small, so that conical diffraction phenomena involve small angles and can be treated paraxially.

In section 2 we describe the paraxial plane waves associated with the two sheets of the wave surface. Application of Hamilton's principle to the phases of these waves (section 3) generates the rays of geometrical optics and the associated light intensity. Section 4 is the formulation of the exact paraxial diffraction theory, based on a 2×2 matrix evolution operator for the action of the crystal on the transverse electric field of the light, regarded as a superposition of plane waves; the result is the same theory as that obtained in a different way by Belsky and Stepanov [16]. Two special cases (section 5) are the pattern in the focal image plane of the incident beam, and

the field on the symmetry axis; in the latter case, the integrals can be evaluated exactly. When the birefringence and optical activity are large, the geometrical field is decorated by a rich interference structure, that can be described in detail (section 6) with explicit and accurate asymptotic approximations for the integrals.

Birefringence is determined by the three principal refractive indices (square roots of principal dielectric constants)

$$n_1 < n_2 < n_3. \tag{1.1}$$

Acting alone, birefringence would generate conical refraction inside the crystal, with cone semi-angle

$$A = \frac{1}{n_2}\sqrt{(n_2 - n_1)(n_3 - n_2)}. \tag{1.2}$$

The value of A is typically a few degrees (0.93° for aragonite, 1.0° for the monoclinic double tungstate crystal $KGd(WO_4)_2$ [6], and 6.9° for naphlalene [17]). If l is the thickness of the crystal, the cone refracts out of the crystal to become a cylinder with radius Al, typically a few millimetres.

Optical activity is specified by the rotation angle γ of a linearly polarized beam travelling along an optic axis of the crystal. The theory to follow is the same whether the optical activity arises intrinsically, that is from microscopic chirality, or is induced by a magnetic field (Faraday effect). Typical values of γ for a 25 mm thick crystal are 2.7π for quartz, 10.3π for α-iodic acid [15], and about 1.1π for the Faraday effect with a field of 1 T in terbium gallium garnet.

The incident beam is specified by its width w, which could represent the radius of an illuminated pinhole or the radius of the waist of a focused Gaussian beam. We will formulate the theory for a general beam profile, and use a Gaussian profile for explicit calculations.

2. Paraxial plane waves

Let the position in the space beyond the crystal be denoted $\{\mathbf{R}, z\}$, where $\mathbf{R}$ represents the transverse position in an observation plane, and z is the distance of the observation plane, measured along the beam direction from an origin at the sharpest focus of the incident beam (for example, pinhole or Gaussian beam waist).

For monochromatic light with vacuum wavenumber k_0, the two plane waves with transverse wavevector components $\mathbf{K}$ can be written

$$\psi_\pm = \exp\left\{\mathrm{i}\left(\mathbf{K}\cdot\mathbf{R} + z\sqrt{k_\pm^2 - K^2}\right)\right\}, \tag{2.1}$$

where the wavenumber in the crystal is given, in terms of the two refractive indices $n_\pm(\mathbf{K})$ corresponding to wave direction $\mathbf{K}$, by

$$k_\pm = k_0 n_\pm(\mathbf{K}). \tag{2.2}$$

The following dimensionless variables will be convenient:

$$\boldsymbol{\rho} = \{\xi, \eta\} = \rho\{\cos\phi, \sin\phi\} \equiv \frac{\mathbf{R}}{w}, \qquad \boldsymbol{\kappa} \equiv w\mathbf{K},$$
$$\rho_0 \equiv \frac{Al}{w}, \qquad \zeta \equiv \frac{l + (z-l)n_2}{n_2 k_0 w^2}. \tag{2.3}$$

$\boldsymbol{\rho}$ is the dimensionless transverse position, measured in units of the beam width, and $\boldsymbol{\kappa}$ is the corresponding transverse wavenumber. With this choice of units, the amplitude of the plane-wave superposition comprising an incident Gaussian beam is particularly simple:

$$a(\kappa) = \exp(-\tfrac{1}{2}\kappa^2). \tag{2.4}$$

ζ is a dimensionless distance, conveniently measured (as will become apparent) from the plane where the focus of the incident beam would be imaged inside the crystal if this were isotropic with index n_2; this 'focal image plane' (section 5.1) is where biaxiality and optical activity generate the sharpest structures in the image (in the pure biaxial case, these are the sharpest Poggendorff rings [5, 6]).

ρ_0 is the dimensionless biaxiality parameter, which together with the chirality parameter γ specifies the crystal. Both parameters can be regarded as phases: γ is the phase associated with chirality, accumulated in the crystal by a circularly polarized wave travelling along the optic axis, and ρ_0 is the phase difference due to birefringence, accumulated by each of the two orthogonal plane eigenwaves travelling in directions making a typical angle $1/k_0 w$ with the z axis in the superposition comprising the incident beam.

With these variables, the direction-dependent refractive indices can be written

$$n_\pm(\mathbf{K}) = n_2(1 + \Delta n_\pm(\boldsymbol{\kappa})), \tag{2.5}$$

where phases associated with the refractive index differences $\Delta n_\pm$ are [7, 8, 18]

$$k_0 n_2 l\,\Delta n_\pm(\boldsymbol{\kappa}) = \pm\sqrt{\kappa^2\rho_0^2 + \gamma^2}. \tag{2.6}$$

For $\gamma = 0$ this describes the double cone, centred on the 'diabolical point' at the optic axis $\boldsymbol{\kappa} = 0$, where the two sheets are connected. For nonzero γ, the sheets are separated.

Extracting the unimportant direction-independent phase factor, the plane waves outside the crystal now become

$$\psi_\pm = \exp\{\mathrm{i}k_0(ln_2 + (z-l))\}\exp\{\mathrm{i}\Phi_\pm(\boldsymbol{\kappa})\}, \tag{2.7}$$

involving the following direction-dependent phases, that will be important in what follows (and in which it is convenient to emphasize only the κ dependence):

$$\Phi_\pm(\boldsymbol{\kappa}) = \boldsymbol{\kappa}\cdot\boldsymbol{\rho} - \tfrac{1}{2}\kappa^2\zeta \mp \sqrt{\kappa^2\rho_0^2 + \gamma^2}. \tag{2.8}$$

3. Geometrical optics

Hamilton's principle determines the direction(s) $\boldsymbol{\kappa}$ of the ray(s) through the point $\boldsymbol{\rho}$, ζ by the requirement that $\Phi_\pm(\boldsymbol{\kappa})$ be stationary:

$$\nabla_{\boldsymbol{\kappa}}\Phi_\pm(\boldsymbol{\kappa}) = 0. \tag{3.1}$$

This gives the condition

$$\boldsymbol{\rho} = \boldsymbol{\rho}_\pm(\boldsymbol{\kappa}) = \boldsymbol{\kappa}\left(\zeta \pm \frac{\rho_0^2}{\sqrt{\rho_0^2\kappa^2 + \gamma^2}}\right), \tag{3.2}$$

which after squaring to eliminate the $\pm$ signs leads to

$$(\rho - \kappa\zeta)^2(\rho_0^2\kappa^2 + \gamma^2) - \kappa^2\rho_0^4 = 0, \tag{3.3}$$

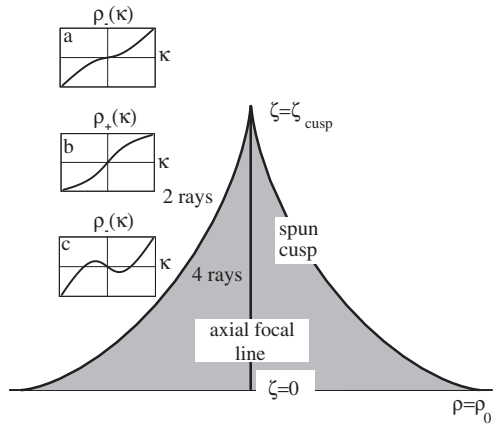

Figure 1. Geometrical optics: spun cusp, axial focal line, numbers of rays, and graphs of (3.2) for (a) $\rho_-(\boldsymbol{\kappa})$ outside the caustic, (b) $\rho_+(\boldsymbol{\kappa})$ everywhere, (c) $\rho_-(\boldsymbol{\kappa})$ inside the caustic.

a quartic equation whose real solutions (labelled by n) give the contributing wavevectors

$$\boldsymbol{\kappa} = \kappa_n(\boldsymbol{\rho}, \zeta)\frac{\boldsymbol{\rho}}{\rho}. \tag{3.4}$$

The intensity of the geometrical-optics field is determined by the Jacobian determinant of the transformation from $\boldsymbol{\kappa}$ to the field point $\boldsymbol{\rho}$ in the observation plane at distance ζ, weighted by the amplitude $a(\boldsymbol{\kappa})$ in the incident beam. The Jacobian is

$$\begin{aligned}\det\left(\frac{\mathrm{d}\boldsymbol{\rho}_\pm}{\mathrm{d}\boldsymbol{\kappa}}\right) &= \left(\zeta \pm \frac{\rho_0^2}{\sqrt{\rho_0^2\kappa^2+\gamma^2}}\right)\left(\zeta \pm \frac{\rho_0^2\gamma^2}{(\rho_0^2\kappa^2+\gamma^2)^{3/2}}\right)\\ &= \frac{\rho}{\kappa}\left(\zeta + \frac{\gamma^2(\rho/\kappa-\zeta)^3}{\rho_0^4}\right),\end{aligned} \tag{3.5}$$

generating the intensity

$$\begin{aligned}I(\boldsymbol{\rho},\zeta) &= \frac{1}{2}\sum_n \left\{|a(\boldsymbol{\kappa})|^2\left|\det\left(\frac{\mathrm{d}\boldsymbol{\rho}_\pm}{\mathrm{d}\boldsymbol{\kappa}}\right)\right|^{-1}\right\}_{\boldsymbol{\kappa}=\boldsymbol{\kappa}_n(\boldsymbol{\rho},\zeta)}\\ &= \frac{1}{2\rho}\sum_n \left\{\kappa|a(\boldsymbol{\kappa})|^2\left(\zeta + \frac{\gamma^2(\rho/\kappa-\zeta)^3}{\rho_0^4}\right)^{-1}\right\}_{\boldsymbol{\kappa}=\boldsymbol{\kappa}_n(\boldsymbol{\rho},\zeta)}.\end{aligned} \tag{3.6}$$

As with any field of rays, the most important places are the caustics, where the Jacobian vanishes and the intensity diverges. This is the locus of multiple roots of the ray equations (3.2) or (3.3). Vanishing of (3.5) together with (3.2), leads to the two types of singularity: an axial focal line

$$\rho = 0, \qquad \zeta \leqslant \frac{\rho_0^2}{\gamma} \equiv \zeta_{\mathrm{cusp}}, \tag{3.7}$$

within, and ending at the cusp of, a circularly symmetric caustic surface—the spun cusp—whose equation is

$$\left(\frac{\rho}{\rho_0}\right)^{2/3} + \left(\frac{\zeta}{\zeta_{\mathrm{cusp}}}\right)^{2/3} = 1. \tag{3.8}$$

Figure 1 illustrates the caustic and the associated ray equations.

We emphasize that the above analysis describes the caustic pattern in the light emerging from the crystal (and, as mentioned already, the corresponding virtual field obtained by continuation). Inside the crystal, the rays have a different structure: a conical caustic if $l/k_0n_2w^2 > \zeta_{\mathrm{cusp}}$, and no caustic if $l/k_0n_2w^2 < \zeta_{\mathrm{cusp}}$ (this internal caustic structure is implicit in the form of the wave surface, discussed in detail by Voigt [13]).

4. Diffraction

The refractive indices (2.6) are eigenvalues of the 2×2 complex Hermitian matrix, acting on the transverse electric $\mathbf{D}$ vector, that generates the eigenpolarizations, and corresponding to the exponential involving $\Phi_\pm(\boldsymbol{\kappa})$ in (2.7) is the 2×2 unitary evolution operator that transforms an arbitrary plane wave. It is convenient to write this as

$$\mathbf{U}(\boldsymbol{\kappa}) = \exp(-\mathrm{i}\mathbf{F}(\boldsymbol{\kappa})) \tag{4.1}$$

where

$$\mathbf{F}(\boldsymbol{\kappa}) = \frac{1}{2}\kappa^2\zeta\mathbf{1} + \rho_0\kappa\begin{pmatrix}\cos\phi_{\boldsymbol{\kappa}} & \sin\phi_{\boldsymbol{\kappa}}\\ \sin\phi_{\boldsymbol{\kappa}} & -\cos\phi_{\boldsymbol{\kappa}}\end{pmatrix} + \gamma\begin{pmatrix}0 & -\mathrm{i}\\ \mathrm{i} & 0\end{pmatrix}. \tag{4.2}$$

It can be confirmed that the eigenvalues of $\mathbf{F}(\boldsymbol{\kappa})$ are $\Phi_\pm(\boldsymbol{\kappa}) - \boldsymbol{\kappa}\cdot\boldsymbol{\rho}$, and the eigenvectors are the polarizations of the two plane waves travelling in direction $\boldsymbol{\kappa}$ in the presence of biaxiality and optical activity, namely

$$\mathbf{d}_\pm(\boldsymbol{\kappa}) = \mathrm{i}\sqrt{\frac{1\pm\Lambda}{2}}\begin{pmatrix}\cos\frac{1}{2}\phi_{\boldsymbol{\kappa}}\\ \sin\frac{1}{2}\phi_{\boldsymbol{\kappa}}\end{pmatrix} \mp \sqrt{\frac{1\mp\Lambda}{2}}\begin{pmatrix}\sin\frac{1}{2}\phi_{\boldsymbol{\kappa}}\\ -\cos\frac{1}{2}\phi_{\boldsymbol{\kappa}}\end{pmatrix}, \tag{4.3}$$

where

$$\Lambda \equiv (1 + (\gamma/\rho_0\kappa)^2)^{-1/2}. \tag{4.4}$$

For nonzero γ, $\mathbf{F}(\boldsymbol{\kappa})$ is a complex Hermitian matrix, so its degeneracies have codimension 3 and so are absent in the two-dimensional space of wave directions $\boldsymbol{\kappa}$; this explains the separation of wave surfaces (2.6). When $\gamma = 0$, $\mathbf{F}(\boldsymbol{\kappa})$ is a real symmetric matrix, so its degeneracies have codimension 2, corresponding to the optic axis at the diabolical point $\boldsymbol{\kappa} = 0$. The eigenvectors (4.3) are multivalued functions of $\boldsymbol{\kappa}$, but of course the electric field $\mathbf{D}$ now to be derived is single valued.

Writing $\mathbf{F}(\boldsymbol{\kappa})$ compactly in terms of Pauli spin matrices, i.e.,

$$\mathbf{F}(\boldsymbol{\kappa}) = \tfrac{1}{2}\kappa^2\zeta\mathbf{1} + \mathbf{V}(\boldsymbol{\kappa})\cdot\mathbf{S}, \tag{4.5}$$

where the vector $\mathbf{V}$ and the vector operator $\mathbf{S}$ are

$$\mathbf{V}(\boldsymbol{\kappa}) = \{\rho_0\kappa\cos\phi_{\boldsymbol{\kappa}}, \rho_0\kappa\sin\phi_{\boldsymbol{\kappa}}, \gamma\}, \qquad \mathbf{S} = \{\boldsymbol{\sigma}_3, \boldsymbol{\sigma}_1, \boldsymbol{\sigma}_2\}, \tag{4.6}$$

brings the evolution operator to the convenient form

$$\begin{aligned}\mathbf{U}(\boldsymbol{\kappa}) &= \exp\left(-\tfrac{1}{2}\mathrm{i}\kappa^2\zeta\right)\\ &\quad\times\left[(\cos|\mathbf{V}(\boldsymbol{\kappa})|)\mathbf{1} - \mathrm{i}\frac{\sin|\mathbf{V}(\boldsymbol{\kappa})|}{|\mathbf{V}(\boldsymbol{\kappa})|}\mathbf{S}\cdot\mathbf{V}(\boldsymbol{\kappa})\right].\end{aligned} \tag{4.7}$$

$\mathbf{U}$ operates on the incident beam, expressed as a superposition of plane waves as

$$\mathbf{D}_0 = \frac{1}{2\pi}\int\int \mathrm{d}\boldsymbol{\kappa}\ \exp(\mathrm{i}\boldsymbol{\kappa}\cdot\boldsymbol{\rho})\mathbf{a}(\boldsymbol{\kappa}), \tag{4.8}$$

where $\mathbf{a}(\boldsymbol{\kappa})$ is the polarization vector of the Fourier component $\boldsymbol{\kappa}$, in the most general case where the polarization can vary across the beam. Then the wave outside the crystal is

$$\mathbf{D} = \frac{1}{2\pi}\int\int \mathrm{d}\boldsymbol{\kappa}\ \exp(\mathrm{i}\boldsymbol{\kappa}\cdot\boldsymbol{\rho})\mathbf{U}(\boldsymbol{\kappa})\mathbf{a}(\boldsymbol{\kappa}). \tag{4.9}$$

To explore the field in more detail, we specialize to the important case where the incident beam has uniform polarization $\mathbf{d}_0$ and is circularly symmetric:

$$\mathbf{a}(\boldsymbol{\kappa}) = a(\kappa)\mathbf{d}_0, \tag{4.10}$$

where, for example $a(\kappa)$ for a Gaussian beam is given by (2.4). Thus the incident beam profile is

$$\mathbf{D}_0 = \int_0^\infty \mathrm{d}\kappa\, \kappa J_0(\kappa\rho) a(\kappa)\mathbf{d}_0. \tag{4.11}$$

Then elementary manipulations lead to the explicit formulae

$$\mathbf{D} = \left[B_0\mathbf{1} + B_1\begin{pmatrix}\cos\phi & \sin\phi\\ \sin\phi & -\cos\phi\end{pmatrix} + B_2\begin{pmatrix}0 & -\mathrm{i}\\ \mathrm{i} & 0\end{pmatrix}\right]\mathbf{d}_0, \tag{4.12}$$

involving the diffraction integrals

$$\begin{aligned}
B_0(\rho,\zeta;\rho_0,\gamma) &= \int_0^\infty \mathrm{d}\kappa\, \kappa a(\kappa)\\
&\quad\times \exp\left(-\tfrac{1}{2}\mathrm{i}\kappa^2\zeta\right) J_0(\kappa\rho)\cos\sqrt{\kappa^2\rho_0^2+\gamma^2}\\
B_1(\rho,\zeta;\rho_0,\gamma) &= \rho_0\int_0^\infty \mathrm{d}\kappa\, \kappa^2 \frac{a(\kappa)}{\sqrt{\kappa^2\rho_0^2+\gamma^2}}\exp\left(-\frac{1}{2}\mathrm{i}\kappa^2\zeta\right)\\
&\quad\times J_1(\kappa\rho)\sin\sqrt{\kappa^2\rho_0^2+\gamma^2} = \frac{\rho_0}{\gamma}\frac{\partial^2}{\partial\rho\partial\gamma}B_0\\
B_2(\rho,\zeta;\rho_0,\gamma) &= -\mathrm{i}\gamma\int_0^\infty \mathrm{d}\kappa\kappa \frac{a(\kappa)}{\sqrt{\kappa^2\rho_0^2+\gamma^2}}\exp\left(-\frac{1}{2}\mathrm{i}\kappa^2\zeta\right)\\
&\quad\times J_0(\kappa\rho)\sin\sqrt{\kappa^2\rho_0^2+\gamma^2} = \mathrm{i}\frac{\partial}{\partial\gamma}B_0.
\end{aligned} \tag{4.13}$$

These expressions are equivalent to those of Belsky and Stepanov [16], who calculate a picture corresponding to linear incident polarization $\mathbf{d}_0$. Here we will not emphasize the polarization pattern, whose implications we have explored elsewhere [19] and which has been observed [15]. Instead, we concentrate on the detailed spatial structure of the field. Therefore it will suffice to give here the wave intensity for unpolarized light, obtained by adding $\mathbf{D}^*\mathbf{D}$ for any two orthogonal polarizations $\mathbf{d}_0$:

$$\begin{aligned}
I(\rho,\zeta;\rho_0,\gamma) &= |B_0(\rho,\zeta;\rho_0,\gamma)|^2\\
&\quad + |B_1(\rho,\zeta;\rho_0,\gamma)|^2 + |B_2(\rho,\zeta;\rho_0,\gamma)|^2.
\end{aligned} \tag{4.14}$$

For the Gaussian beams (2.4) commonly employed nowadays, the 'complex-source' trick [20] enables the integrals B_m to be written in terms of functions of three variables rather than four. The trick is based on the substitution

$$\zeta \to \zeta - \mathrm{i}, \tag{4.15}$$

and leads to

$$\begin{aligned}
B_0(\rho,\zeta;\rho_0,\gamma) &= \frac{C_0(u,u_0,\gamma)}{1+\mathrm{i}\zeta}\\
B_1(\rho,\zeta;\rho_0,\gamma) &= \frac{C_1(u,u_0,\gamma)}{1+\mathrm{i}\zeta}\\
B_2(\rho,\zeta;\rho_0,\gamma) &= \frac{C_2(u,u_0,\gamma)}{1+\mathrm{i}\zeta},
\end{aligned} \tag{4.16}$$

where, in terms of the variables

$$u \equiv \frac{\rho}{\sqrt{1+\mathrm{i}\zeta}}, \qquad u_0 \equiv \frac{\rho_0}{\sqrt{1+\mathrm{i}\zeta}}, \tag{4.17}$$

the diffraction integrals C_m are

$$\begin{aligned}
C_0(u,u_0,\gamma) &= \int_0^\infty \mathrm{d}s\, sJ_0(su)\\
&\quad\times \exp\left(-\tfrac{1}{2}s^2\right)\cos\sqrt{s^2u_0^2+\gamma^2}\\
C_1(u,u_0,\gamma) &= u_0\int_0^\infty \mathrm{d}s\, s^2\frac{J_1(su)}{\sqrt{s^2u_0^2+\gamma^2}}\\
&\quad\times \exp\left(-\tfrac{1}{2}s^2\right)\sin\sqrt{s^2u_0^2+\gamma^2} = \frac{u_0}{\gamma}\frac{\partial^2}{\partial u\partial\gamma}C_0\\
C_2(u,u_0,\gamma) &= -\mathrm{i}\gamma\int_0^\infty \mathrm{d}s\, s\frac{J_0(su)}{\sqrt{s^2u_0^2+\gamma^2}}\\
&\quad\times \exp\left(-\tfrac{1}{2}s^2\right)\sin\sqrt{s^2u_0^2+\gamma^2} = \mathrm{i}\frac{\partial}{\partial\gamma}C_0.
\end{aligned} \tag{4.18}$$

These integrals converge and can be evaluated numerically. Figure 2 shows intensity patterns in the ρ, ζ plane, for several values of ρ_0 and γ. The ray structure described in section 3, with the cusped caustic containing an axial focal line, is evident, but in this paraxially exact theory the geometrical features are decorated with interference.

5. Special cases

5.1. Focal image plane ($\zeta = 0$)

In this case the variables u and u_0 are real, and the C_m integrals (4.18) are equal to the B_m integrals (4.13). The integrals cannot be evaluated in closed form, but are easily computed. Figure 3 shows the light intensity as a function of ρ for different values of optical activity γ and a fixed large value of ρ_0. For $\gamma \ll \rho_0$, the focal image shows the two sharp bright rings, separated by the Poggendorff dark ring, characteristic of conical diffraction in the absence of chirality. As γ increases, many additional rings develop, and the pattern spreads towards smaller ρ, associated with the approach towards the focal image plane of the cusp at $\zeta_\mathrm{cusp} = \rho_0^2/\gamma$.

5.2. On the axis ($\rho = 0$)

Here the argument of the Bessel functions in the integrals C_m vanishes, and the transformation

$$s \equiv \sqrt{2t^2 - \frac{\gamma^2}{u_0^2}}, \tag{5.1}$$

from s to a new integration variable t, leads easily to the following expressions for the C_m in terms of complementary

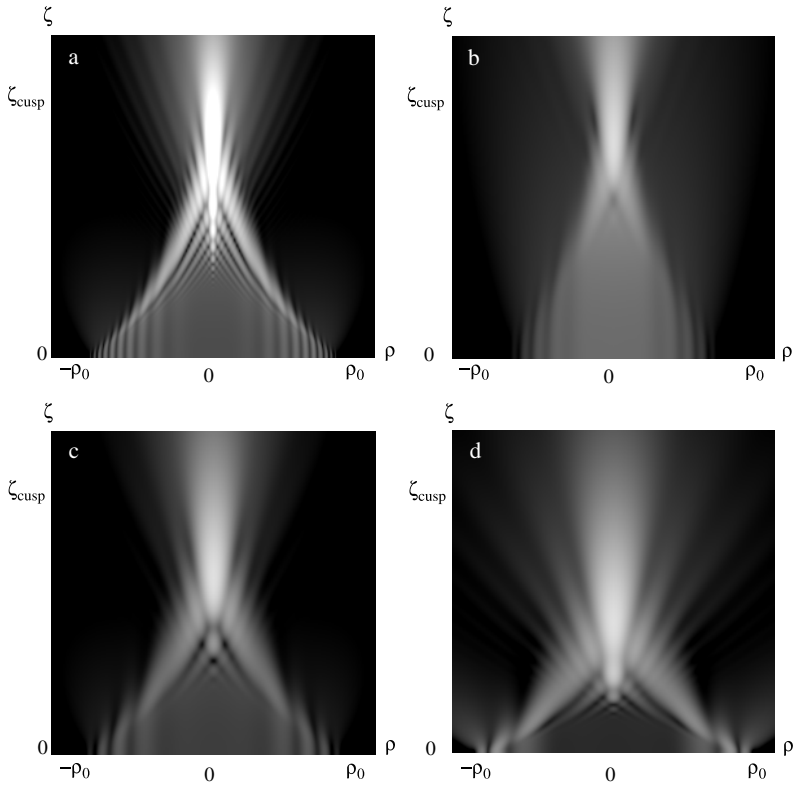

Figure 2. Density plots of intensity for unpolarized incident light, computed from integrals in section 4, for (a) $\rho_0 = \gamma = 50$, (b) $\rho_0 = 20$, $\gamma = 40$, (c) $\rho_0 = \gamma = 20$, (d) $\rho_0 = 20$, $\gamma = 10$.

error functions:

$$C_0(0,u_0,\gamma) = \cos\gamma + \mathrm{i}\frac{u_0\sqrt{\pi}}{2\sqrt{2}}\exp\left(\frac{\gamma^2}{2u_0^2} - \frac{u_0^2}{2}\right) \times \left[\mathrm{erfc}\left(\frac{\gamma/u_0 - \mathrm{i}u_0}{\sqrt{2}}\right) - \mathrm{erfc}\left(\frac{\gamma/u_0 + \mathrm{i}u_0}{\sqrt{2}}\right)\right]$$

$$C_1(0,u_0,\gamma) = 0 \qquad (5.2)$$

$$C_2(0,u_0,\gamma) = -\frac{\gamma\sqrt{\pi}}{2u_0\sqrt{2}}\exp\left(\frac{\gamma^2}{2u_0^2} - \frac{u_0^2}{2}\right) \times \left[\mathrm{erfc}\left(\frac{\gamma/u_0 - \mathrm{i}u_0}{\sqrt{2}}\right) - \mathrm{erfc}\left(\frac{\gamma/u_0 + \mathrm{i}u_0}{\sqrt{2}}\right)\right].$$

Figure 4 shows the corresponding intensities, calculated using (4.14), (4.16) and (4.17). When $\rho_0 \gg 1$ and $\gamma \gg 1$, there is a maximum near $\zeta/\zeta_{\mathrm{cusp}} = 1$. As γ decreases, keeping ρ_0 large, the maximum moves to smaller ζ, until when $\gamma/\rho_0 \ll 1$ it approaches the maximum for $\gamma = 0$, namely [6] $\zeta \sim \sqrt{2/3}\rho_0 \equiv \zeta_{\mathrm{max}}$, i.e., $\zeta/\zeta_{\mathrm{cusp}} \sim \sqrt{2/3}\gamma/\rho_0$.

This behaviour can be understood in terms of the asymptotics of the error functions. Labelling the arguments of erfc in (5.2) as A_- and A_+, the two erfc terms correspond to a single integral over $\exp(-u^2)$ in the complex plane, from A_- to A_+. For $\zeta \gg 1$, A_+ is asymptotically close to the line $\arg u = \pi/4$ and its contribution decays as $1/\zeta$ and can be neglected (it corresponds to the single ray labelled + in (3.2)). When $0 \ll \zeta < \zeta_{\mathrm{cusp}}$, then, as in the non-chiral case [5], the axial intensity asymptotics is dominated (apparently paradoxically [21]) by the subdominant exponential in (5.2). This comes from the saddle point $u = 0$ of the integrand, and contributes the main axial spike, with maximum at ζ_{max}. The dominant exponential comes from the endpoint A_-. As ζ approaches ζ_{cusp}, this contribution diverges as $1/(\zeta_{\mathrm{cusp}} - \zeta)$. Then A_- crosses a Stokes line [22] which eliminates the saddle-point contribution, after which the intensity decays linearly. If $\gamma > \rho_0\sqrt{(3/2)}$, i.e., $\zeta_{\mathrm{max}} > \zeta_{\mathrm{cusp}}$, the subdominant exponential never reaches its maximum.

6. Asymptotics

6.1. Stationary phase

For large values of ρ_0 and/or γ, the integrands in B_{m} (equations (4.13)) oscillate rapidly, and so the integrals can be approximated by the method of stationary phase. The real contributing points $\boldsymbol{\kappa}_n$ (solutions of (3.3)) correspond to the rays (3.4) of geometrical optics: four inside the spun cusp, and two outside. These give not only the amplitude associated with each ray (square root of the intensity in (3.6), generated by the Jacobian (3.5)), but also the interferences between them. Outside the spun cusp, there are two complex solutions of the ray equation (3.3), of which the one with the positive value of $\mathrm{Im}\,\Phi(\boldsymbol{\kappa})$ represents an exponentially small evanescent wave—the ghostly remnant of the two rays that have coalesced on the caustic.

The simplest way to determine these contributions is to consider a point $\boldsymbol{\rho}$ on the x axis, and work not with (4.13) but with the two-dimensional integrals (4.9), approximating the integral over κ_y first and then that over κ_x. This

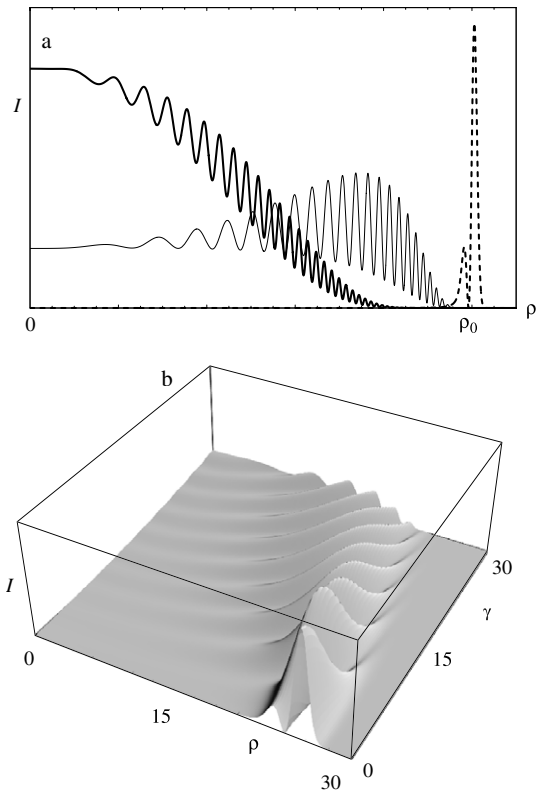

Figure 3. (a) Exact intensity in the focal plane (section 5.1) for $\rho_0 = 100$; dashed curve: $\gamma = 0$ (intensity reduced by a factor 6); thin curve: $\gamma = 100$; thick curve: $\gamma = 200$. (b) 3D plot of intensity as a function of ρ and γ, for $\rho_0 = 25$.

procedure allows negative stationary values of κ_x and enables unambiguous determination of the phases $\pm\pi/4$ associated with each integration, and leads to

$$B_m(\rho,\zeta;\rho_0,\gamma) \approx \frac{1}{2\sqrt{\rho}}\sum_n \frac{F_m(\kappa_n)a(\kappa_n)}{\sqrt{|D(\kappa_n)|}} \times \exp\{\mathrm{i}(\delta(\kappa_n)+\Phi(\kappa_n))\}$$

$$D(\kappa) = -\zeta - \frac{\gamma^2}{\rho_0^4}\left(\frac{\rho}{\kappa}-\zeta\right)^3,$$

$$\delta(\kappa) = \tfrac{1}{2}(\arg\kappa - \arg D(\kappa)) \qquad (6.1)$$

$$\Phi(\kappa) = \kappa\rho - \frac{1}{2}\kappa^2\zeta - \frac{\rho_0^2}{(\rho/\kappa-\zeta)}$$

$$F_0(\kappa) = 1, \qquad F_1(\kappa) = \frac{\kappa}{\rho_0}\left(\frac{\rho}{\kappa}-\zeta\right)$$

$$F_2(\kappa) = \frac{\gamma}{\rho_0^2}\left(\frac{\rho}{\kappa}-\zeta\right).$$

Inside the caustic, the sum over n contains four real-ray terms. Outside, there are the two real-ray terms, and the one evanescent-wave term that is present in the region between two sets of Stokes lines outside the caustic. For fixed ρ_0 and γ, the Stokes lines [22, 23] are the loci in the ρ, ζ plane where the real part of the phase of the evanescent contribution equals the (already real) phase of one of the two real rays. For diffraction

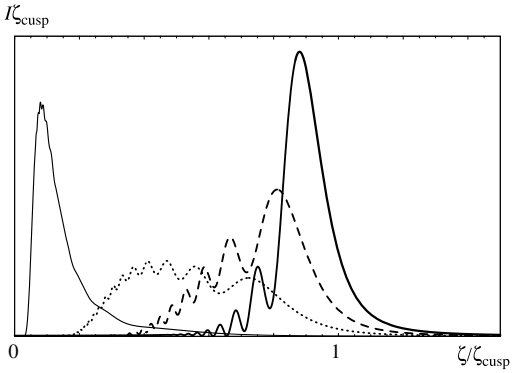

Figure 4. Intensity on the axis (section 5.2) $\rho_0 = 100$ and $\gamma = 10$ (thin curve), $\gamma = 50$ (dotted curve), $\gamma = 100$ (dashed curve), and $\gamma = 200$ (thick curve).

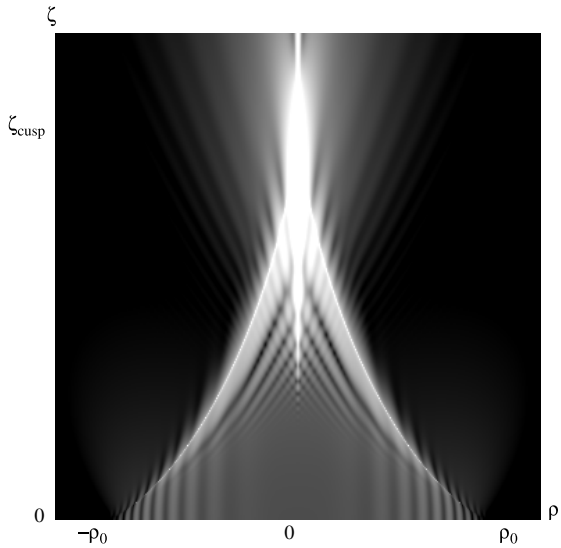

Figure 5. As in figure 2(a), calculated by stationary phase (section 6.1), including the evanescent wave outside the caustic.

decorating the standard cusp [24], the Stokes lines also form a cusp, wider than the caustic cusp and sprouting from this on the opposite side. The corresponding analysis in the present case is given in appendix A.

Figure 5 shows the intensity given by this stationary-phase method and including the evanescent wave. Comparison with figure 2(a) shows that all interference features are correctly reproduced, though of course the approximation diverges on the cusped caustic and the axial focal line, where two or more stationary points κ_n coincide.

6.2. Near the cusp

The most dramatic failure of stationary phase occurs in the neighbourhood of the cusp point $\rho = 0$, $\zeta = \zeta_{\mathrm{cusp}}$, where all four stationary points coincide. A simplification is possible in this region, by mapping the integrals B_{m} onto the simplest function with the same symmetry and the same deportment of stationary points. This is the 'spun cusp diffraction catastrophe':

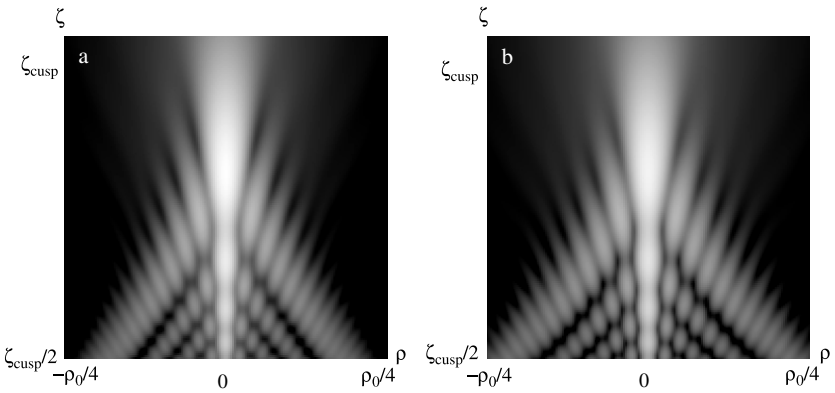

Figure 6. (a) Intensity near the cusp for $\rho_0 = \gamma = 100$, computed numerically from the integrals in section 4; (b) as (a), computed using the spun cusp approximation of section 4.

$$J(x, y) = \int_0^\infty \mathrm{d}t\, t \exp\{-\mathrm{i}(t^4 + xt^2)\} J_0(yt), \tag{6.2}$$

which can be regarded as a modification, incorporating circular symmetry, of the familiar Pearcey integral [25, 26] that describes diffraction associated with planar cusps. Numerical approximation of (6.2) is facilitated by choosing a contour receding to $t = \infty \exp(-\mathrm{i}\pi/8)$ (Kirk *et al* [27] call J the Bessoid integral).

The mapping is a simplification because it approximates three functions of four variables $(\rho, \zeta, \rho_0, \gamma)$ in terms of an integral that depends only on two.

The mapping is most simply derived by replacing the variable κ in the B_m integrals by t according to

$$\kappa(t) = t\left(\frac{8\gamma^2}{\rho_0^2(\zeta - \mathrm{i})}\right)^{1/4} \sqrt{1 + \frac{t^2\rho_0}{\gamma\sqrt{2(\zeta - \mathrm{i})}}}. \tag{6.3}$$

For B_0 this gives, exactly,

$$\begin{aligned} B_0(\rho, \zeta; \rho_0, \gamma) = {} & \int_0^\infty \mathrm{d}t\, t \left(\frac{\gamma}{\rho_0}\sqrt{\frac{8}{\zeta - \mathrm{i}}} + t^2\frac{4}{\zeta - \mathrm{i}}\right) \\ & \times \exp\left\{-\mathrm{i}\left(t^4 + t^2\frac{\gamma}{\rho_0}\sqrt{2(\zeta - \mathrm{i})}\right)\right\} \\ & \times \cos\left(\gamma + \rho_0 t^2\sqrt{\frac{2}{\zeta - \mathrm{i}}}\right) J_0(\kappa(t)\rho). \end{aligned} \tag{6.4}$$

This can be expressed in terms of $J(x, y)$ simply by approximating the function $\kappa(t)$ in the Bessel function by its linear part, corresponding to replacing the outer square root in (6.3) by unity. Then with the definitions

$$\begin{aligned} x_\pm &\equiv \sqrt{2}\left(\frac{\gamma\sqrt{\zeta - \mathrm{i}}}{\rho_0} \mp \frac{\rho_0}{\sqrt{\zeta - \mathrm{i}}}\right), \\ y &\equiv \rho\left(\frac{8\gamma^2}{\rho_0^2(\zeta - \mathrm{i})}\right)^{1/4}, \end{aligned} \tag{6.5}$$

the diffraction integrals become

$$\begin{aligned} B_0(\rho, \zeta; \rho_0, \gamma) \approx {} & \frac{\gamma}{\rho_0}\sqrt{\frac{2}{\zeta - \mathrm{i}}} \\ & \times \left(1 + \mathrm{i}\frac{\rho_0}{\gamma}\sqrt{\frac{2}{\zeta - \mathrm{i}}}\frac{\partial}{\partial x}\right)[\exp(\mathrm{i}\gamma) J(x_+, y) \\ & + \exp(-\mathrm{i}\gamma) J(x_-, y)] \\ B_1(\rho, \zeta; \rho_0, \gamma) \approx {} & \mathrm{i}\frac{2^{5/4}}{(\zeta - \mathrm{i})^{3/4}}\sqrt{\frac{\gamma}{\rho_0}}\frac{\partial}{\partial y}[\exp(\mathrm{i}\gamma) J(x_+, y) \\ & - \exp(-\mathrm{i}\gamma) J(x_-, y)] \\ B_2(\rho, \zeta; \rho_0, \gamma) \approx {} & -\frac{\gamma}{\rho_0}\sqrt{\frac{2}{(\zeta - \mathrm{i})}}[\exp(\mathrm{i}\gamma) J(x_+, y) \\ & - \exp(-\mathrm{i}\gamma) J(x_-, y)]. \end{aligned} \tag{6.6}$$

At the cusp point itself, exact evaluation of $J(0, 0)$ and $\partial_x J(0, 0)$ and substitution into (6.6) leads, for $\gamma \gg 1$ (i.e., when the cusp is fully developed) to the intensity

$$I(\rho = 0, \zeta = \zeta_{\mathrm{cusp}}) \approx \frac{\pi\gamma^3}{4\rho_0^4}. \tag{6.7}$$

The extraordinary accuracy of the spun cusp approximation (6.6) in capturing the wave near the caustic and the axial focal line is illustrated in figure 6. The only errors arise for small ζ, where the approximation decorates not the true geometrical caustic (3.8) but the following approximation to it, that gets more accurate as ζ approaches ζ_{cusp}:

$$\frac{\rho}{\rho_0} \approx \sqrt{\frac{\zeta_{\mathrm{cusp}}}{\zeta}}\left[\frac{2}{3}\left(1 - \frac{\zeta}{\zeta_{\mathrm{cusp}}}\right)\right]^{3/2}. \tag{6.8}$$

It is probably possible to fix this error by a mapping more sophisticated than (6.3), but this is unnecessary because the approximation in the following section deals with the caustic, including the region far below ζ_{cusp} where (6.6) begins to fail.

6.3. Near the caustic

For $\zeta < \zeta_{\mathrm{cusp}}$ and away from the axial focal line (i.e., ρ not small), the stationary phase approximation fails in the simplest way, by two of the four real stationary points coinciding

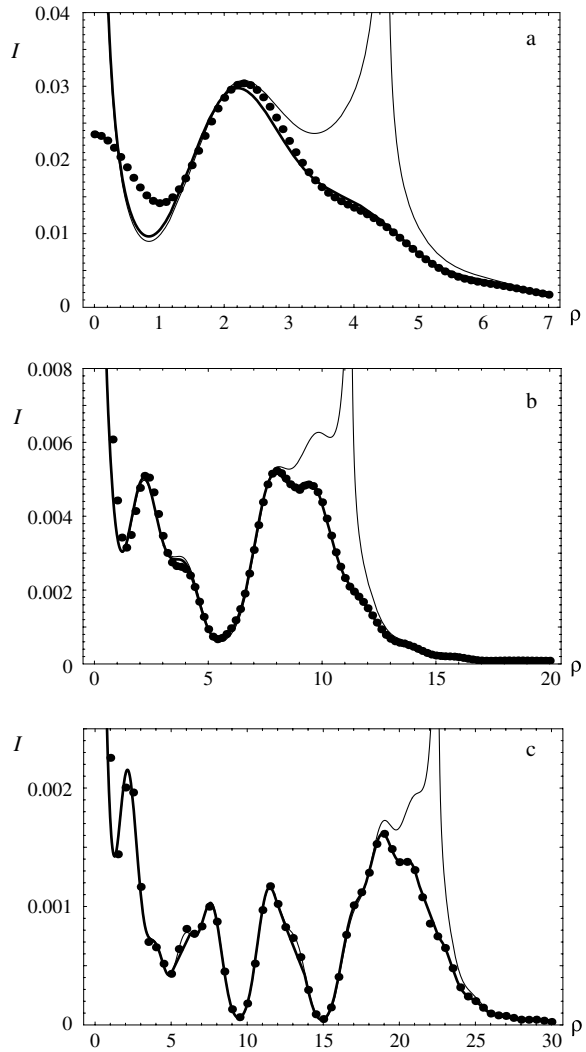

Figure 7. Full curves: uniform Airy approximation for intensity I (section 6.3 and appendix B) for (a) $\rho_0 = \gamma = 20$, $\zeta = \zeta_{\text{cusp}}/2 = 10$, (b) $\rho_0 = \gamma = 50$, $\zeta = \zeta_{\text{cusp}}/2 = 25$, (c) $\rho_0 = \gamma = 100$, $\zeta = \zeta_{\text{cusp}}/2 = 50$; dots: exact computations (section 4); thin curves: stationary phase approximation (section 6.1), including evanescent waves as well as the real rays of geometrical optics.

on the caustic. The standard remedy is the technique of uniform approximation [28, 29], in which the integrand is matched to a cubic exponential capturing the topology of stationary-point coalescence, leading to an approximation in terms of the Airy function $\text{Ai}(x)$ [30] and its derivative. Rather than repeating the usual derivation, we give in appendix B a simplified argument demonstrating the inevitability of the formulae in a form that can be applied immediately, using only geometrical quantities appearing in the bare stationary phase approximation.

Figure 7 shows how accurate the uniform approximation is, when applied to the two coalescing stationary phase contributions to (6.1) according to the recipe (A.13), even when ρ_0 and γ are not large.

7. Concluding remarks

The richness of the diffraction pattern outside a chiral biaxial crystal is surprising. Its dominant geometric features (section 3), emerging clearly from the exact integrals (section 4) when the dimensionless parameters ρ_0 and γ are large, are the spun cusp caustic and the axial focal line threading it. Describing the local details requires both elementary and sophisticated asymptotics. Away from the caustic, the simple method of stationary phase (section 6.1) endows the geometrical rays with phase, explaining much of the interference, as well as the evanescent waves outside (appendix A). On the axis, the asymptotics involves error functions (section 5.2); across the caustic, matching to Airy functions is required (section 6.3); and the region near the spun cusp point requires a rotationally symmetric modification of the Pearcey function (section 6.2). In all cases, the philosophy is the same: to simplify the exact general theory by describing the local phenomena with functions of fewer variables.

These caustic and interference phenomena, predicted by theory, have not been observed. In the only detailed experimental study known to us [15], observations were restricted to a single plane, namely the exit face of the crystal; this is close to the focal image plane (in our notation, $\zeta \sim 1$, and the experiment corresponded to parameters $\rho_0 \sim \gamma \sim 20$), so the spun cusp and axial focal line were not apparent. With this present paper, we hope to stimulate further experimental study, complementing and extending our recent detailed comparison of experiment with theory [6] for conical diffraction in the non-chiral case.

The theory reported here does not exhaust the physics associated with Hamilton's remarkable discovery, because we have still not included anisotropic absorption. This will restore the degeneracy that chirality eliminated, which will reappear not as the original double-cone ('diabolical') intersection of wave surfaces at the optic axis but as a pair of branch-points—the 'singular axes' [7]. We are exploring the influence of this radically different mathematical structure on an incident light beam, and will report the results later. A further extension, especially appropriate to thick crystals, involves nonlinearity, and considerable progress has been made in formulating the theory for this case [31].

Acknowledgments

MVB's and MRJ's researches are supported by the Royal Society.

Appendix A. Stokes lines

With the new coordinates u, v and the new variable τ, defined by

$$u \equiv \frac{\rho}{\rho_0}, \qquad v \equiv \frac{\zeta}{\zeta_{\text{cusp}}}, \qquad \tau \equiv u - \frac{v\rho_0}{\gamma}\kappa, \tag{A.1}$$

the ray equation (3.3) takes the simpler form

$$(\tau - u)^2(\tau^2 - 1) + v^2\tau^2 = 0, \tag{A.2}$$

the caustic (3.8) becomes

$$u^{2/3} + v^{2/3} = 1, \tag{A.3}$$

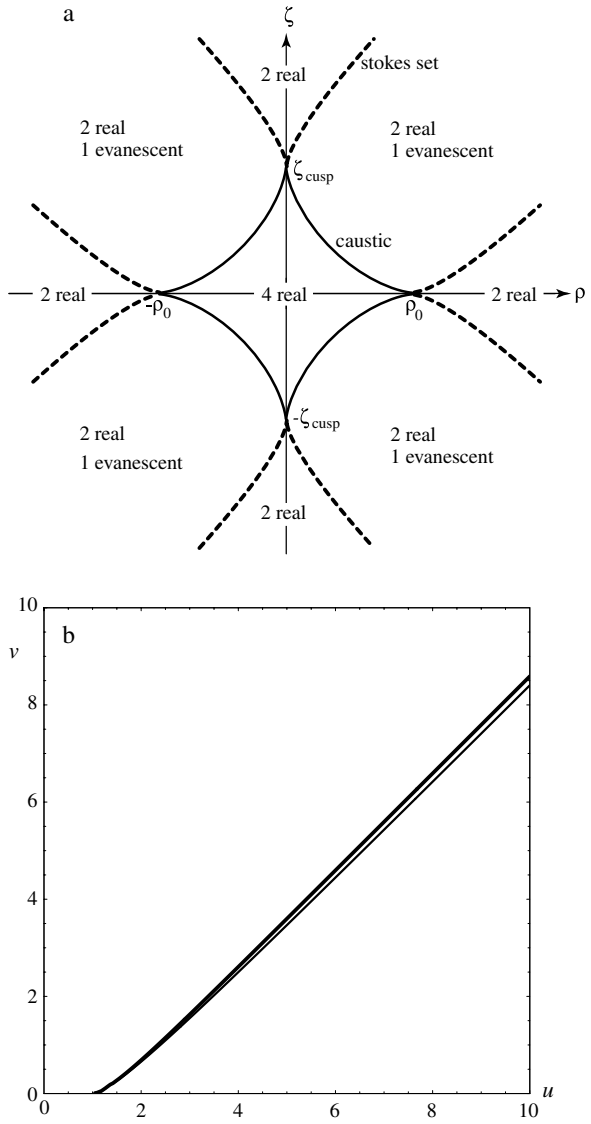

Figure A.1. (a) Caustic (full) and Stokes lines (dashed), indicating the number of real and evanescent waves in each region. (b) Exact Stokes line (thick) and approximation (A.6) (thin).

and, after removing irrelevant τ-independent constants and using (A.2), both phases (2.8) can be written in the common form

$$\Phi_\pm(\boldsymbol{\kappa}) \equiv \phi(\tau;u) = -\frac{1}{2}\tau^2 - \frac{u}{\tau}. \tag{A.4}$$

Let the roots of the quartic equation (A.2) be $\tau_n(u,v)$ ($n = 1,2,3,4$), where $n = 1,2$ refer to the two roots that coincide on the caustic and become complex conjugates outside, and $n = 3,4$ refer to the roots that are real everywhere, and denote the corresponding phases by $\phi(\tau_n(u,v),u) = \phi_n(u,v)$. Then in the region outside the caustic that we are interested in, that is $u^{2/3} + v^{2/3} > 1$, $\phi_2 = \phi_1^*$ and both ϕ_3 and ϕ_4 are real.

The condition for a Stokes line, that the real part of either of the complex phases equals either of the real ones, can be written in the following convenient form, free of explicit stipulations of real parts and without $\pm$ signs:

$$\left[\tfrac{1}{2}(\phi_1(u,v)+\phi_2(u,v)) - \phi_3(u,v)\right] \times \left[\tfrac{1}{2}(\phi_1(u,v)+\phi_2(u,v)) - \phi_4(u,v)\right] = 0. \tag{A.5}$$

Figure A.1(a) shows the full real and complex ray structure in the ρ, ζ plane, including the Stokes lines numerically computed from (A.5). We have not been able to find an explicit analytic expression for the Stokes lines, but an accurate approximation, illustrated in figure A.1(b), is obtained by interpolating between the exact Stokes lines near and far from the cusp:

$$v^2 - \frac{a(u-1)^3}{1+a(u-1)} = 0, \qquad \text{where } a = \frac{10}{27} + \frac{2}{3\sqrt{3}}. \tag{A.6}$$

(This represents just one of the eight branches of the Stokes lines in figure A.1(a); the others are easily obtained by changing signs and interchanging u and v.)

Appendix B. Elementary derivation of uniform Airy approximation

This is a simplified derivation, using physical arguments, complementing the standard mathematical derivation [28].

Consider a function depending on some variables, that we do not need to specify, described approximately (for example, by stationary phase) in a region R by the superposition of two exponentials ('waves'), that is

$$f_{\text{statonary phase}} = a_1 \exp\{\mathrm{i}(\phi_1 + \tfrac{1}{4}\pi)\} + a_2 \exp\{\mathrm{i}(\phi_2 - \tfrac{1}{4}\pi)\}, \tag{A.7}$$

where ϕ_1 and ϕ_2 are real, with the convention

$$\phi_2 > \phi_1 \tag{A.8}$$

(so that in the stationary phase approximation ϕ_2 corresponds to a maximum and ϕ_1 to a minimum, justifying the signs of the phases $\pi/4$).

In the situation envisaged here, ϕ_1 approaches ϕ_2 near the boundary ('caustic') of R, on which their values coincide and the amplitudes a_1 and a_2 diverge, so that the approximation (A.7) fails. Outside R, ϕ_1 and ϕ_2 are complex conjugates of each other, and f involves the exponential whose Im ϕ is larger ('evanescent wave').

Now we argue that a better approximation, curing the divergence on the boundary of R, and therefore uniformly valid near and far from the boundary, is obtained by representing f as a superposition of Ai and its derivative Ai$'$, as follows:

$$f_{\text{uniform}} = \exp\{\tfrac{1}{2}\mathrm{i}(\phi_1+\phi_2)\}[P\,\mathrm{Ai}(-x) + Q\,\mathrm{Ai}'(-x)], \tag{A.9}$$

involving the unknown quantities P and Q and the argument

$$x = (\tfrac{3}{4}(\phi_2 - \phi_1))^{2/3}. \tag{A.10}$$

Only this form is capable of reproducing (A.7) far from the boundary of R, via the Airy asymptotic formulae

$$\mathrm{Ai}(-x) \approx \frac{\sin(\frac{2}{3}x^{3/2} + \frac{1}{4}\pi)}{x^{1/4}\sqrt{\pi}}, \qquad \mathrm{Ai}'(-x) \approx \frac{x^{1/4}\cos(\frac{2}{3}x^{3/2} + \frac{1}{4}\pi)}{\sqrt{\pi}}. \tag{A.11}$$

The requirement that (A.9) reproduces (A.7) exactly in the geometrical-optics regime fixes P and Q uniquely as

$$P = x^{1/4}\sqrt{\pi}(a_1 + a_2), \qquad Q = \frac{\mathrm{i}}{x^{1/4}}\sqrt{\pi}(a_1 - a_2). \tag{A.12}$$

Thus the uniform approximation, superseding (A.7), is

$$f_{\text{uniform}} = \sqrt{\pi}\,\exp\{\tfrac{1}{2}\mathrm{i}(\phi_1+\phi_2)\} \times\left[x^{1/4}(a_1+a_2)\mathrm{Ai}(-x)+\frac{\mathrm{i}}{x^{1/4}}(a_1-a_2)\mathrm{Ai}'(-x)\right]. \tag{A.13}$$

We note that this formula involves only quantities appearing in the less accurate version (A.7). Moreover, (A.13) also reproduces the single evanescent-wave contribution outside R, where $\phi_1-\phi_2$ is imaginary, when (A.10) is interpreted to make the Airy argument $-x$ positive.

References

[1] Hamilton W R 1837 Third supplement to an essay on the theory of systems of rays *Trans. R. Irish. Acad.* **17** 1–144

[2] Lloyd H 1833 On the phaenomena presented by light in its passage along the axes of biaxial crystals *Phil. Mag.* **2** 112–20
Lloyd H 1833 *Phil. Mag.* **2** 207–10

[3] Born M and Wolf E 1959 *Principles of Optics* (London: Pergamon)

[4] Belskii A M and Khapalyuk A P 1978 Internal conical refraction of bounded light beams in biaxial crystals *Opt. Spectrosc. (USSR)* **44** 436–9

[5] Berry M V 2004 Conical diffraction asymptotics: fine structure of Poggendorff rings and axial spike *J. Opt. A: Pure Appl. Opt.* **6** 289–300

[6] Berry M V, Jeffrey M R and Lunney J G 2006 Conical diffraction: observations and theory *Proc. R. Soc.* A at press

[7] Ramachandran G N and Ramaseshan S 1961 Crystal optics *Handbuch der Physik* vol XXV/I, ed H Flügge (Berlin: Springer)

[8] Berry M V and Dennis M R 2003 The optical singularities of birefringent dichroic chiral crystals *Proc. R. Soc.* A **459** 1261–92

[9] Berry M V 2005 The optical singularities of bianisotropic crystals *Proc. R. Soc.* A **461** 2071–98

[10] Berry M V 2004 Physics of nonhermitian degeneracies *Czech. J. Phys.* **54** 1040–7

[11] Poggendorff J C 1839 Ueber die konische refraction *Pogg. Ann.* **48** 461–2

[12] Voigt W 1905 Bemerkung zur theorie der konischen refraktion *Phys. Z.* **6** 672–3

[13] Voigt W 1905 Theoretisches und experimentelles zur aufklärung des optisches verhaltens aktiver kristalle *Ann. Phys.* **18** 645–94

[14] Portigal D L and Burstein E 1972 Effect of optical activity or Faraday rotation on internal conical refraction *J. Opt. Soc. Am.* **62** 859–64

[15] Schell A J and Bloembergen N 1978 Laser studies of internal conical diffraction. II. Intensity patterns in an optically active crystal, α-iodic acid *J. Opt. Soc. Am.* **68** 1098–106

[16] Belsky A M and Stepanov M A 2002 Internal conical refraction of light beams in biaxial gyrotropic crystals *Opt. Commun.* **204** 1–6

[17] Raman C V, Rajagopalan V S and Nedungadi T M K 1941 Conical refraction in naphlalene crystals *Proc. Ind. Acad. Sci.* A **14** 221–7

[18] Landau L D, Lifshitz E M and Pitaevskii L P 1984 *Electrodynamics of Continuous Media* (Oxford: Pergamon)

[19] Berry M V, Jeffrey M R and Mansuripur M 2005 Orbital and spin angular momentum in conical diffraction *J. Opt. A: Pure Appl. Opt.* **7** 685–90

[20] Deschamps G A 1971 Gaussian beam as a bundle of complex rays *Electron. Lett.* **7** 684–5

[21] Berry M V 2004 Asymptotic dominance by subdominant exponentials *Proc. R. Soc.* A **460** 2629–36

[22] Heading J 1962 *An Introduction to Phase-Integral Methods* (London: Methuen)

[23] Berry M V 1989 Uniform asymptotic smoothing of Stokes's discontinuities *Proc. R. Soc.* A **422** 7–21

[24] Wright F J 1980 The Stokes set of the cusp diffraction catastrophe *J. Phys. A: Math. Gen.* **13** 2913–28

[25] Pearcey T 1946 The structure of an electromagnetic field in the neighbourhood of a cusp of a caustic *Phil. Mag.* **37** 311–7

[26] Berry M V and Upstill C 1980 Catastrophe optics: morphologies of caustics and their diffraction patterns *Prog. Opt.* **18** 257–346

[27] Kirk N P, Connor J N L, Curtis P R and Hobbs C A 2000 Theory of axially symmetric cusped focusing: numerical evaluation of a Bessoid integral by an adaptive contour algorithm *J. Phys. A: Math. Gen.* **33** 4797–808

[28] Chester C, Friedman B and Ursell F 1957 An extension of the method of steepest descents *Proc. Camb. Phil. Soc.* **53** 599–611

[29] Wong R 1989 *Asymptotic Approximations to Integrals* (New York: Academic)

[30] Abramowitz M and Stegun I A 1972 *Handbook of Mathematical Functions* (Washington, DC: National Bureau of Standards)

[31] Newell A 2005 private communication